Journal of *Marine Science and Engineering*

MDPI

Article

Tsunami Risk Change Analysis for Qidong County of China Based on Land Use Classification

Jingming Hou [1,2], Yi Gao [1,2], Tingting Fan [1], Peitao Wang [1,2], Yuchen Wang [3], Juncheng Wang [1] and Wei Lu [1,*]

[1] National Marine Environmental Forecasting Center, Beijing 100081, China
[2] Key Laboratory of Marine Hazards Forecasting, Ministry of Natural Resources, Beijing 100081, China
[3] Japan Agency for Marine-Earth Science and Technology, Yokohama 236-0001, Japan
* Correspondence: luwei68@foxmail.com

Abstract: Tsunamis can cause high numbers of casualties, as well as direct and indirect economic losses to coastal regions. The huge destructiveness of tsunamis requires us to study tsunami risk and its temporal change. We adopt the tsunami scenarios of the Ryukyu Trench as an example to analyze the temporal change in tsunami risk. According to the tsunami numerical model results, the tsunami inundation in the worst tsunami scenario covered an area of 82.83 km^2. Satellite data including Landsat 8 images from July 2013 and Landsat 9 images from March 2022 were used with the random forest (RF) method to analyze land use and tsunami vulnerability in 2013 and 2022. The tsunami risk and its temporal change were analyzed by integrating tsunami hazard and tsunami vulnerability. The tsunami risk change analysis results show that the area of tsunami risk level 1 increased by 4.57 km^2, and the area of tsunami risk level 4 decreased by 7.31 km^2. By analyzing changes in land use and land cover (LULC) and tsunami risk, we concluded that the expansion of constructed land and the increase in coastal population were responsible for the increase in tsunami risk. The results of tsunami risk change analysis will help us understand the current tsunami risk and predict possible future risk change. In addition, it is necessary to prepare tsunami prevention measures in advance and produce tsunami emergency response plans for Qidong County and other regions under potential tsunami threat.

Keywords: random forest; tsunami risk; vulnerability; remote sensing

Citation: Hou, J.; Gao, Y.; Fan, T.; Wang, P.; Wang, Y.; Wang, J.; Lu, W. Tsunami Risk Change Analysis for Qidong County of China Based on Land Use Classification. *J. Mar. Sci. Eng.* **2023**, *11*, 379. https://doi.org/10.3390/jmse11020379

Academic Editor: Efim Pelinovsky

Received: 23 December 2022
Revised: 31 January 2023
Accepted: 1 February 2023
Published: 8 February 2023

1. Introduction

A tsunami is a sudden natural disaster with short duration, but it may have a lasting impact on the affected region. Although a large tsunami is a relatively rare event, it is one of the most devastating and deadly coastal disasters, often causing great loss of life. On 26 December 2004, the Indian Ocean tsunami [1], with a maximum tsunami runup of 50.9 m, killed more than 220,000 people. This tsunami destroyed thousands of buildings, industries, bridges, and other manmade infrastructure, making it one of the most destructive tsunamis in history. The tsunami waves hit many countries around the Indian Ocean, causing great damage and leaving 1.5 million people homeless. The 2011 Japan tsunami [2–4], with a tsunami runup of 38.9 m, killed 18,000 people. The tsunami, in combination with a series of disasters and accidents caused by it, resulted in devastating damage to parts of northeast Japan. Historically, there have been several major tsunami events, including the 1755 Lisbon tsunami [5] and the 1964 Alaska Tsunami [6]. In addition, tsunamis are also triggered by landslides and volcanic eruptions. Two non-seismic tsunamis have occurred since 2011, the 2018 Indonesia tsunami [7] and the 2022 Tonga tsunami [8].

Previous tsunami research has been conducted to understand the characteristics of tsunami hazard [9–12]. The management of future tsunami risk requires a good understanding of the disaster. According to natural disaster system theory, tsunami risk in a given region should take into account both the tsunami hazard and the tsunami vulnerability of the affected objects (population and infrastructure). Quantifying the vulnerability

of affected objects is important for tsunami risk assessment. Tsunami risk assessment results could help to understand the impact of a tsunami before its arrival. In general, historical tsunami records are too limited to conduct a purely empirical disaster assessment. Therefore, tsunami risk assessment needs to use a combination of numerical modeling and observation data to assess tsunami risk. In the last two decades, tsunami risk assessment methods have experienced substantial growth. Two popular methods are the deterministic risk assessment [13,14] and the probabilistic risk assessment [15]. The deterministic tsunami assessment considers the worst-case tsunami scenario, analyzes the tsunami hazard (wave height, inundation area, and flow velocity), and calculates the tsunami risk in combination with tsunami vulnerability. The worst-case earthquake scenarios are associated with seismic dip–slip motion [16]. The probabilistic tsunami risk assessment considers all possible tsunami events to estimate the probability of a wave height at a particular location above a threshold level over a certain period. This method provides a likelihood of occurrence and return periods [17].

In recent years, a substantial amount of research on new methods and technologies for tsunami risk assessment has been conducted. Some studies have highlighted the potential of remote sensing techniques in tsunami risk assessment [18]. Since 2004, remote sensing has been used in many tsunami studies. Remote sensing technologies and data are used in combination with other data to analyze tsunami hazard, vulnerability, and risk. The application of remote sensing in tsunami risk assessment includes providing input for tsunami numerical calculations, tsunami damage monitoring, and tsunami vulnerability analysis. The bathymetry data derived from remote sensing can be used as input bathymetry data for tsunami numerical models. Land use data can be used to analyze coefficients of friction in tsunami models [19]. Satellite images can also be used for rapid, large-scale damage detection to understand the scale of tsunamis, especially in affected areas that cannot be reached immediately after a tsunami disaster [19]. A number of important input parameters for vulnerability analysis were derived from remote sensing [20,21].

Land use and land cover (LULC) is a classic concept and key parameter for understanding the relationship between humans and the environment [22]. Remote sensing data are often used to monitor LULC change [23,24]. LULC changes are related to the catastrophic effects of disasters. Understanding changes in LULC and their regional distribution is critical to addressing a variety of environmental and natural disaster issues [25]. Over the past half a century, more and more free satellite imagery data and improved classification technologies have been made available. The Landsat 8 satellite was launched in February 2013 and has provided data for nearly a decade [26]. The new generation Landsat 9 satellite was launched in September 2021 [27]. At present, the Operational Land Imager (OLI) and OLI2 sensors regularly observe the global land surface. The Landsat images with a resolution of 30 m have been widely used in ecosystem variation research [28], disaster prevention and mitigation [29], and detailed LULC mapping [30] because of their rich archives and free availability [31]. In previous literature, Landsat images and their spectral indices were often used for LULC classifications [32].

With rapid global urbanization, the population living in coastal areas is increasing, and economic assets are becoming concentrated in the region. Tsunami risk change means the change in tsunami risk of a certain area over time. Paulik developed a spatiotemporal loss model to quantify the changes in tsunami risk to residential buildings over a 20-year period [33]. Qidong County, located on the southeast coast of China, is facing the threat of both transoceanic and regional tsunamis, especially tsunamis from the Ryukyu Trench. The purpose of this paper is to analyze the change in tsunami risk for Qidong County, China, from 2013 to 2022, considering the worst tsunami scenario of Ryukyu Trench. LULC classification results were used to analyze tsunami vulnerability. Tsunami risk and risk change were analyzed in combination with tsunami hazard and tsunami vulnerability.

2. Materials and Methods

2.1. Study Area

Qidong County is located at the southeastern tip of Jiangsu Province on the north bank of the Yangtze River Estuary. It is bordered by the sea and surrounded by water on three sides. Figure 1a shows the location of Qidong County, which is only approximately 50 km away from Shanghai. Important marine aquaculture areas exist off the coast of Qidong. The terrain of Qidong County is flat, slightly higher in the northwest and lower in the southeast. The ground elevation is between 2.0 and 5.0 m. Such flat terrain is vulnerable to potential tsunami events. Ports and marine aquaculture areas may suffer significant losses.

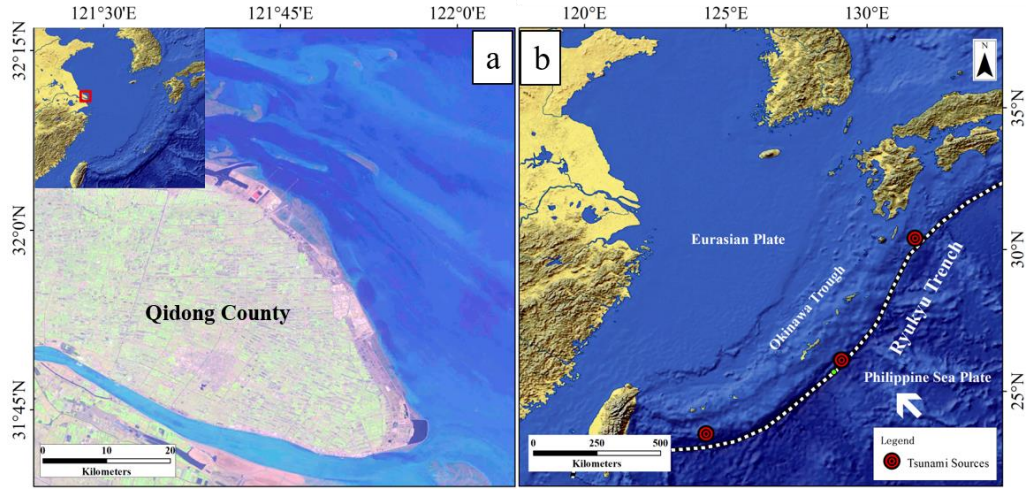

Figure 1. (**a**) Location of Qidong County. (**b**) Location of the potential tsunami sources considered in this study.

Historically, there have been several tsunamis in the surrounding areas of Qidong and Shanghai. On 9 July 1498, an earthquake occurred in Japan and triggered a tsunami. Similar tsunami disasters have been observed in Jiangsu, Shanghai, and other areas of China. On 24 December 1854, an earthquake of magnitude 8.4 occurred in Nankaido, Japan and caused a tsunami, which spread to the Jiangsu and Zhejiang provinces of China. According to the historical county chronicle, the river suddenly rose by nearly 1 m, and there were huge waves near the sea. After the 2011 Tohoku earthquake, a tsunami was observed on the coast of Jiangsu Province and Shanghai. Although no observational data were available in Qidong County, tide gauges in Shanghai recorded a tsunami height of ~20 cm with a long-lasting resonance [34].

The most dangerous tsunami source affecting Qidong is from the Ryukyu Trench. The Ryukyu Trench is located on the eastern side of the Ryukyu Islands, which stretch from Japan to Taiwan [35], being approximately 1000 km in length. The southern section of the trench is deepest, with a maximum depth of 7507 m. The Ryukyu Trench is the boundary between the Eurasian Plate and the Philippine Sea Plate. At the location of the Ryukyu Trench, the Philippine Sea Plate subducts north-westwards below the Eurasian Plate at a rate of 8 cm per year [36].

Earthquakes in the Ryukyu Trench could trigger tsunamis [36]. Historically, there have been several earthquakes with magnitudes more than 8.0 in the Ryukyu Trench. The most influential earthquakes include the Yaeyama earthquake in 1771 and the earthquake near Kikai in 1911 [37]. On 24 April 1771, an earthquake struck near the Yaeyama Islands in the southern Ryukyu Islands. Although the ground shaking was relatively weak, the following tsunami was devastating. The southeast coast of Ishigaki Island recorded a tsunami runup of 30 m. The tsunami runup observed in the Yaeyama and Miyako Islands exceeded 10 m. Approximately 12,000 people were killed on Yaeyama and Miyako Islands.

Historical tsunamis have occurred in several locations of the Ryukyu Trench. Therefore, this study assumed three sources in the northern, middle, and southern sections of the

Ryukyu Trench, as shown in Figure 1b. The worst-case scenarios with a magnitude of 9.0 were considered. The source parameters were set according to the local historical earthquakes.

2.2. Data Materials and Preprocessing

The Landsat satellite images from sensors OLI and OLI2 were used in this study. The satellite data were from the Collection 2 level 1 dataset (https://earthexplorer.usgs.gov/: accessed on 12 August 2022). The OLI imagery acquisition time was 12 July 2013 and the OLI2 imagery acquisition time was 23 March 2022, as shown in Table 1. The Landsat images provide 30 m spatial resolution with a revisit time of 16 days, including four visible bands, one near-infrared (NIR) band, and two short-wavelength infrared (SWIR) bands. Landsat imagery preprocessing includes radiometric calibration and atmospheric correction. Radiation calibration was conducted to eliminate the error produced by variations in sensor performance and characteristics over time. The atmospheric correction was then implemented to obtain surface reflectance.

Table 1. Datasets used in the study.

Satellite	Sensor	Acquisition Date	Spatial Resolution	Bands	Path/Row	Data Sources
Landsat 8	OLI	12 July 2013	30 m	1–7	118/038	https://earthexplorer.usgs.gov/
Landsat 9	OLI2	23 March 2022	30 m	1–7	118/038	https://earthexplorer.usgs.gov/

In addition to seven bands, we also considered the spectral indices related to LULC types, including the normalized difference vegetation index (*NDVI*), modification of normalized difference water index (*MNDWI*), normalized difference building index (*NDBI*) and bare soil index (*BSI*).

NDVI is related to the photosynthetic potential of vegetation, which is widely used to quantify vegetation density [38]. *NDVI* was developed by Rousse [39], and takes into consideration the red band and the near-infrared band.

$$NDVI = \frac{\rho_{NIR} - \rho_{RED}}{\rho_{NIR} + \rho_{RED}} \quad (1)$$

where ρ_{RED} and ρ_{NIR} are Band 4 and Band 5 of OLI/OLI2, respectively.

MNDWI is a water index, which was developed by Xu [40]. *MNDWI* can improve the accuracy when identifying water features [41]. It uses the green band and the short-wave infrared bands.

$$MNDWI = \frac{\rho_{GREEN} - \rho_{SWIR}}{\rho_{GREEN} + \rho_{SWIR}} \quad (2)$$

where ρ_{GREEN} and ρ_{SWIR} are Band 3 and Band 6 of OLI/OLI2, respectively.

The *NDBI* [42] is an index developed to rapidly extract urban fabric. The method considers the unique spectral responses of built-up areas and other land covers. The formula is as follows:

$$NDBI = \frac{\rho_{SWIR} - \rho_{NIR}}{\rho_{SWIR} + \rho_{NIR}} \quad (3)$$

where ρ_{SWIR} and ρ_{NIR} are Band 6 and Band 5 of OLI/OLI2, respectively.

Rikimaru proposed the *BSI* in 1996 [43]. *BSI* is a numerical indicator that combines blue, red, near-infrared, and short-wave infrared spectral bands to capture soil variations. The formula of *BSI* is as below:

$$BSI = \frac{((\rho_{RED} + \rho_{SWIR}) - (\rho_{NIR} + \rho_{BLUE}))}{((\rho_{RED} + \rho_{SWIR}) + (\rho_{NIR} + \rho_{BLUE}))} \quad (4)$$

where ρ_{RED}, ρ_{BLUE}, ρ_{NIR}, and ρ_{SWIR} are Band 4, Band 2, Band 5, and Band 6 of OLI/OLI2, respectively.

2.3. Methodology

In this study, tsunami risk and its temporal change were analyzed by combining tsunami hazard and tsunami vulnerability. The tsunami numerical model was used to calculate tsunami inundation. The calculation results were analyzed for tsunami hazard. Landsat images were used to classify LULC and analyze tsunami vulnerability. The technical flowchart of this study is shown in Figure 2.

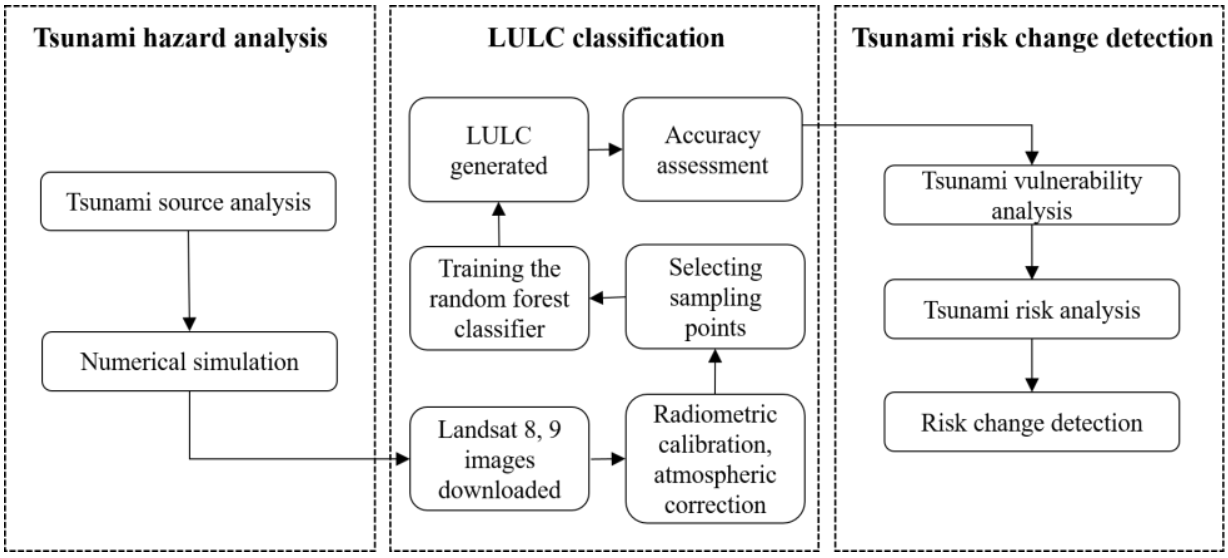

Figure 2. Overall flowchart of this study.

The COMCOT model was used for tsunami hazard analysis. The COMCOT model is a type of long-wave simulation model developed by Cornell University. It can simulate the entire process of tsunami from generation to propagation and inundation. The governing equations are shallow-water equations, which are solved by explicit staggered leap-frog finite difference schemes in both spherical and cartesian coordinates. A nested grid system can be used to fulfill the need for tsunami simulations at different scales. The accuracy and applicability of the model were verified through the simulation of historical tsunami events, such as the 1960 Chilean tsunami [44] and the 2004 Indian Ocean tsunami [45].

In the tsunami vulnerability analysis, machine learning (ML) was used for LULC classification. Recently, a variety of techniques have been developed to improve LULC classification accuracy [46]. ML classifiers are popular due to their ability to use training samples to classify satellite images [47]. Common ML classifiers include the random forest (RF), extreme Gradient boosting (XGBoost), k-nearest neighbor (k-NN), and support vector machine (SVM) [48]. The RF method was used for LULC mapping in this study.

The RF classifier was introduced by Breiman [49]. It is regarded as an ensemble learning algorithm. The key to RF is to create a set of decision trees. The RF classifier uses a set of decision trees to make a prediction and applies a voting mechanism to the results. RF allows the training and classification process to be highly parallelized to reduce the overfitting phenomenon. Therefore, it is widely used in LULC monitoring [50]. We use the Python language scikit-learn library to establish an RF model. This study set the number of decision trees in the random forest to 200.

3. Tsunami Risk Change Analysis

3.1. Tsunami Hazard Analysis

In COMCOT, the following nonlinear shallow-water equations are implemented in spherical coordinates as

$$\frac{\partial \eta}{\partial t} + \frac{1}{Rcos\varphi}\left\{\frac{\partial P}{\partial \psi} + \frac{\partial}{\partial \varphi}(cos\varphi Q)\right\} = -\frac{\partial h}{\partial t} \quad (5)$$

$$\frac{\partial P}{\partial t} + \frac{1}{Rcos\varphi}\frac{\partial}{\partial \psi}\left\{\frac{P^2}{H}\right\} + \frac{1}{R}\frac{\partial}{\partial \varphi}\left\{\frac{PQ}{H}\right\} + \frac{gH}{Rcos\varphi}\frac{\partial \eta}{\partial \psi} - fQ + F_x = 0 \quad (6)$$

$$\frac{\partial Q}{\partial t} + \frac{1}{Rcos\varphi}\frac{\partial}{\partial \psi}\left\{\frac{PQ}{H}\right\} + \frac{1}{R}\frac{\partial}{\partial \varphi}\left\{\frac{Q^2}{H}\right\} + \frac{gH}{R}\frac{\partial \eta}{\partial \varphi} + fP + F_y = 0 \quad (7)$$

where H is the total water depth and $H = \eta + h$. η is the water surface elevation, h is the water depth, R is the radius of the Earth, and g represents the gravitational acceleration. P and Q denote the volume fluxes in longitudinal (ψ) direction and latitudinal (φ) direction, f is the Coriolis force, Fx and Fy denote the bottom friction in longitudinal direction and latitudinal direction, respectively. This tsunami numerical model used a four-layer nested grid, which is shown in Table 2.

Table 2. Nested grids of numerical model.

Layers	Longitude and Latitude	Spatial Resolution	Grids
Layer 1	−60.0°–70.0°N, 100.0°–300.0° E	4′	2999 × 2623
Layer 2	31.3°–34.5° N, 119.5°–122.6° E	1′	188 × 232
Layer 3	31.5°–33.1 N°, 120.7°–122.2° E	1/4′	356 × 452
Layer 4	31.6°–32.1 N°, 121.4°–122.0° E	1/32′	1208 × 1112

The results of the tsunami numerical calculation of layer 1 are shown in Figure 3. The maximum tsunami amplitude reaching the coast of Qidong County is more than 3 m. The tsunami numerical results show that tsunami inundation occurred in the coastal area of Qidong County. The tsunami scenario that had the largest inundation areas in Qidong County was selected. This tsunami source is located in the middle section of the Ryukyu Trench. The numerical result of layer 4 was used to analyze tsunami inundation. This study classified tsunami hazards into four levels according to the tsunami inundation depth, as given in Table 3. Level 1 indicates the greatest tsunami inundation, while level 4 is the lowest inundation level.

Table 3. Classification of tsunami hazard.

Levels	Inundation Depth (m)
1	(3.0, +∞)
2	(1.0, 3.0]
3	(0.3, 1.0]
4	(0, 0.3]

According to the numerical results and tsunami hazard levels shown in Figure 4, 82.83 km^2 of coastal areas were inundated under the tsunami scenario of a magnitude 9.0 earthquake in the middle of the Ryukyu Trench. The maximum tsunami inundation depth was more than 3 m, classified as a hazard of level 1. There were villages, communities, transport terminals, parks, schools, companies, temples, and hotels in the inundation area. A variety of LULC types were in the inundation area, including cropland, woodland, built-up land, and water.

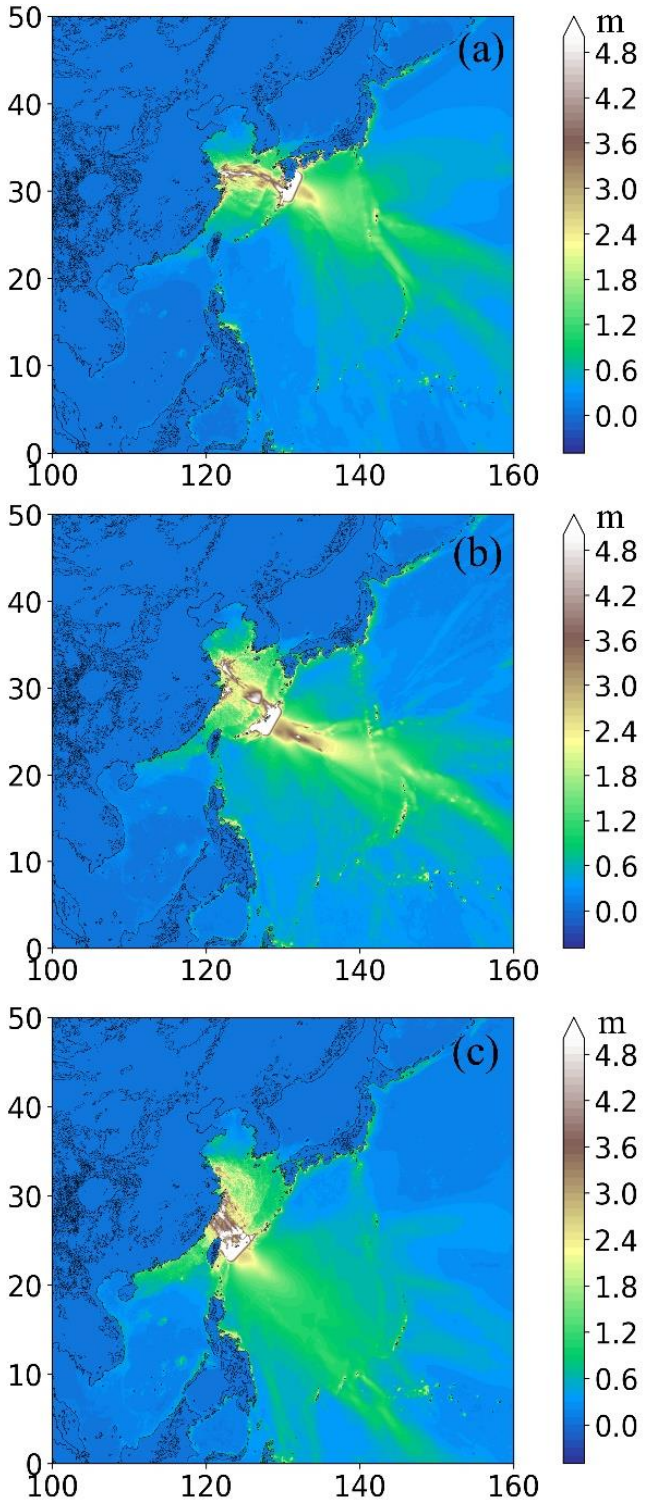

Figure 3. The maximum tsunami amplitude of layer 1: (**a**) tsunami source in the northern part of the Ryukyu Trench, (**b**) tsunami source in the middle of the Ryukyu Trench, (**c**) tsunami source in the southern part of the Ryukyu Trench.

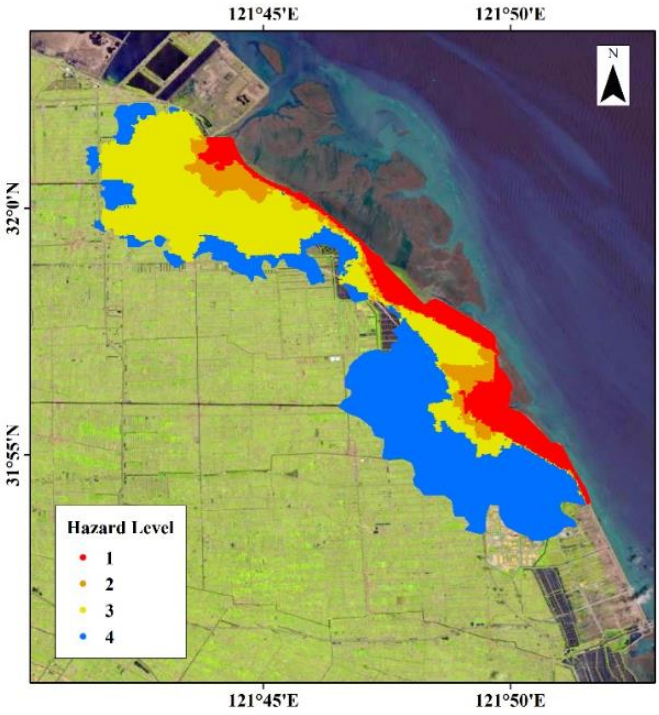

Figure 4. Tsunami hazard levels.

3.2. Tsunami Vulnerability Analysis

3.2.1. Supervised Classification with Random Forest

The RF method was used for the LULC classification. We collected ground truth samples in the inundation area of Qidong County through field observation, including 257 samples from 2013 and 336 samples from 2022.

Several optical band combinations of Landsat 8 and 9, which are often used to distinguish ground objects, were used for LULC classification. Spectral indices were also used in LULC classifications. The band combinations and spectral indices are shown in Table 4.

Table 4. Band combinations used in this study.

Options	Bands	Bands No.
A	Coastal, Blue, Green, Red, NIR, SWIR 1, SWIR 2	1,2,3,4,5,6,7
B	Blue, Green, Red, NIR, SWIR 1	2,3,4,5,6
C	Blue, Green, Red	2,3,4
D	Green, Red, NIR	3,4,5
E	Blue, NIR, SWIR 1	2,5,6
F	Red, NIR, SWIR 1	4,5,6
G	Optimal bands + Spectral index	Optimal bands + Spectral index

The sample training was conducted according to the different combinations (Table 4). Option G selected the best option from the previous options, and then combined it with each spectral index to find the optimal bands and index combination. The spectral indices used included *NDVI*, *MNDWI*, *NDBI*, and *BSI*.

To evaluate the accuracy of the classification results under different options, we calculated the classification accuracy. The *F*1 score was used to test the accuracy.

$$Precision = \frac{TP}{TP + FP} \tag{8}$$

$$Recall = \frac{TP}{TP + FN} \tag{9}$$

$$F1 = \frac{2 \cdot Precision \cdot Recall}{Precision + Recall} \tag{10}$$

where TP is the number of true positives, FP indicates the number of false positives, and FN is the number of false negatives. The precision is the classifier's ability to not label negative samples as positive, and the recall evaluates the classifier's ability to find all positive samples. The relative contribution of precision and recall to the $F1$ score are equal. The best value of the $F1$ score is 1 and the worst value is 0.

The $F1$ scores for 2013 are shown in Figure 5. The scores of cropland and built-up land are relatively high, and the scores of water and bare land are lower. After adding the spectral index of *MNDWI*, the $F1$ score of water increases. After comparison, Scheme G scored the highest, followed by Scheme E. Therefore, we applied Scheme G (i.e., a combination of bands 2, 5, 6, and *MNDWI*) for LULC classification in 2013.

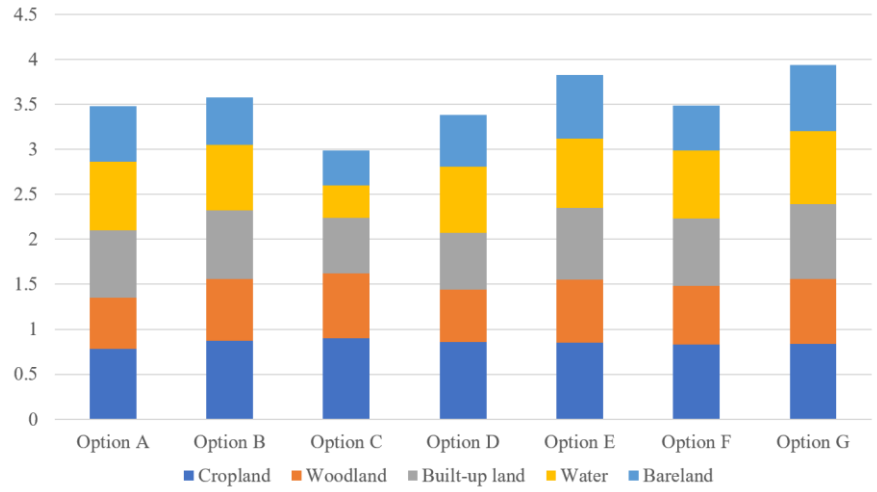

Figure 5. F1 scores for 2013.

The $F1$ scores for 2022 are shown in Figure 6. The cropland and built-up land scored higher, and the scores of woodland and bare land were relatively low. With the addition of *NDVI*, the $F1$ score of woodland and bare land increases. Option G performed best. Therefore, the combination of bands 4, 5, and 6 plus *NDVI* in scheme G was chosen for LULC classification in 2022.

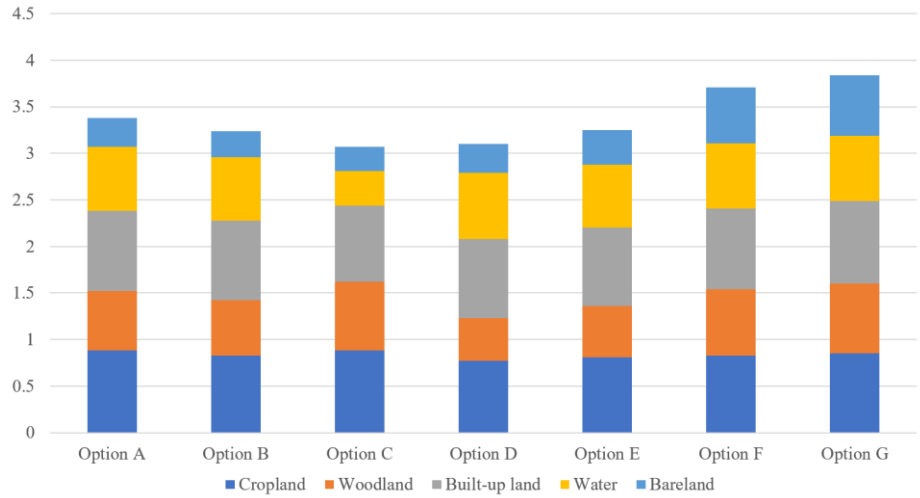

Figure 6. $F1$ scores for 2022.

The acquisition period for Landsat 8 imagery was the summer of 2013, while the Landsat 9 imagery acquisition period was the spring of 2022. The *F*1 scores show that LULC classification could be conducted using different band combinations in different seasons. Option G with a spectral index performed well in both 2013 and 2022, indicating that a suitable spectral index could improve the classification accuracy.

The LULC classification results for 2013 and 2022 are shown in Table 5 [51]. After analysis, the area of built-up land and woodland increased, while the area of cropland, bare land, and water decreased in the inundation area of Qidong County. The change in built-up land is obvious, with an increase of 16.62 km^2. Of the new built-up land, 6% used to be bare land, 21% used to be cropland, 29% used to be woodland, and 44% used to be water.

Table 5. Results of LULC classification.

LULC Types	2013 (km^2)	2022 (km^2)	Change (km^2)	Vulnerability
Cropland	17.0	15.13	−1.87	2
Woodland	18.78	19.40	+0.62	3
Built-up land	16.50	33.12	+16.62	1
Water	27.03	14.83	−12.20	3
Bare land	3.52	0.35	−3.17	4

3.2.2. Tsunami Vulnerability Analysis

The term 'vulnerability' in natural disaster science refers to the vulnerability of disaster-affected objects [52]. It is defined as the ability of disaster-affected objects to withstand different degrees of damage and to compensate for the damage and return to normal level. Vulnerability assessment is an analysis of the disaster-bearing capacity of disaster-affected objects under the conditions of natural disasters of a specific intensity. In this study, we performed a tsunami vulnerability classification based on the results of LULC classification. The correspondence between LULC types and vulnerability levels was established and the vulnerability assessment was conducted using LULC types as the disaster-affected objects. The classification criteria are shown in Table 5. The vulnerability level was divided into four levels, with level 4 being the lowest vulnerability.

The vulnerability analysis results of tsunami inundation area in Qidong County are shown in Table 6, counting the area of all vulnerability levels. According to Tables 5 and 6, the areas with high vulnerability in Qidong County were urban residential and commercial land with intensive human economic and social activities, as well as agricultural land related to production activities. The areas with the lowest vulnerability were water, bare land, and woodland, which were not closely related to human activities.

Table 6. Results of tsunami vulnerability analysis.

Vulnerability Levels	2013 (km^2)	2022 (km^2)	Change (km^2)
1	16.50	33.12	+16.62
2	17.00	15.13	−1.87
3	45.81	34.23	−11.58
4	3.52	0.35	−3.17

From the vulnerability change in Table 6, we can see that areas at vulnerability level 1 increased by 16.62 square kilometers. As the economy develops, the area of building land increases, and the corresponding tsunami vulnerability will increase. The level 4 vulnerability decreased, and there was less bare land.

3.3. Tsunami Risk Change Analysis

Based on the results regarding tsunami hazard and tsunami vulnerability, we analyzed the tsunami risk and its temporal change. The tsunami risk of a specified scenario is a function of its hazard and vulnerability. The tsunami risk level was determined according

to the hazard levels and vulnerability levels [53] (Table 7). The tsunami risk assessment results provide scientific reference for policy makers to manage and reduce the risk of disaster from a potential tsunami event.

Table 7. The criteria of tsunami risk levels.

Hazard	Vulnerability			
	Level 4	Level 3	Level 2	Level 1
Level 4	4	4	3	3
Level 3	4	3	2	2
Level 2	3	2	2	1
Level 1	3	2	1	1

A convenient and effective way of representing tsunami risk levels is tsunami risk maps. These maps show the extent of areas with defined risk levels (e.g., high, medium, and low). Risk maps can be derived using Geographic Information System technology to integrate tsunami hazard and vulnerability map layers. The results of the tsunami risk analysis for 2013 and 2022 are shown in Figure 7. The tsunami risk in the inundation area of Qidong County could be divided into four levels, denoted by red (level 1), orange (level 2), yellow (level 3), and blue (level 4).

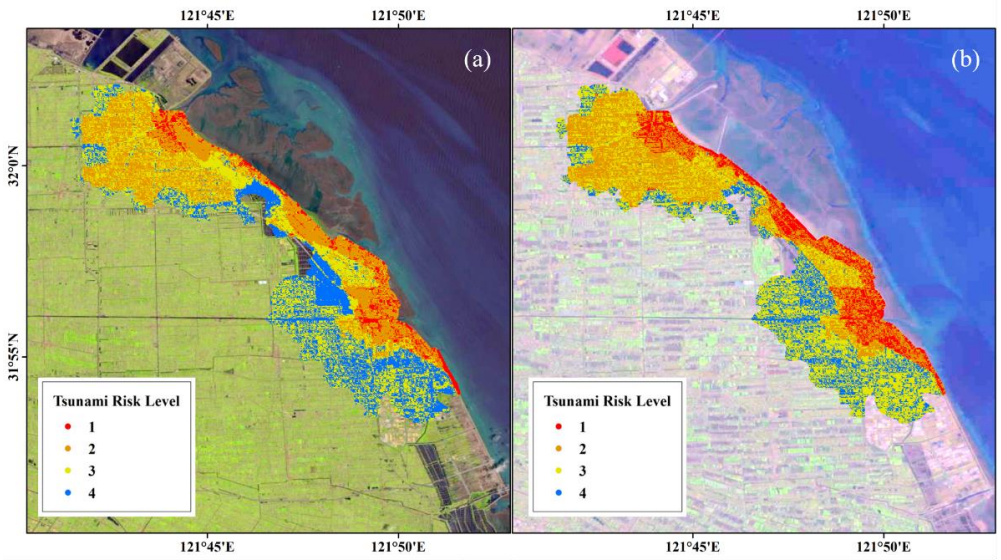

Figure 7. (**a**) Tsunami risk levels for 2013. (**b**) Tsunami risk levels for 2022.

In general, the tsunami risk levels along the coast of Qidong County were high. Areas further from the coast were at lower tsunami risk. The tsunami risk change in Qidong County is shown in Table 8. The area at tsunami risk level 1 increased by 4.57 km^2, while the area at level 4 decreased by 7.31 km^2. Hence, we conclude that economic development and urbanization have led to an increase in tsunami risk. The area at tsunami risk level 1 increased mainly in coastal areas, which are the main areas for the expansion of built-up land.

Table 8. Tsunami risk change from 2013 to 2022.

Risk Levels	2013 (km^2)	2022 (km^2)	Change (km^2)
1	3.58	8.15	+4.57
2	25.88	26.10	+0.22
3	32.07	34.59	+2.52
4	21.29	13.98	−7.31

4. Discussion

With the ongoing rapid economic development, increasing numbers of people and important facilities are being concentrated in coastal areas. Tsunami risk and its temporal change require more attention. This study discussed the tsunami risk change in Qidong County from 2013 to 2022.

Our results suggest that the tsunami risk of Qidong County is generally high in cases of potential earthquakes in the Ryukyu Trench. Meanwhile, economic development and urbanization have led to an increase in tsunami risk. Hence, disaster prevention and mitigation efforts need to be strengthened to address increased tsunami risk in Qidong County. Relevant tsunami mitigation measures need to be developed, including strengthening tsunami risk assessments, conducting research on disaster prevention measures for important disaster affected objects, and formulating tsunami emergency and evacuation plans in advance.

This paper has several limitations. (1) This paper analyzed the change in tsunami risk based on change in land use and vulnerability, assuming that tsunami inundation remains unchanged. Tsunami risk change with a change in inundation areas needs to be analyzed in the future. (2) The Landsat imagery used in this paper is a long-term data source available at present. Data sources with higher resolution will be considered in the future. (3) This study used the land use factor to analyze the change in tsunami vulnerability and tsunami risk. However, tsunami vulnerability involves some other factors, such as ecological vulnerability, economic vulnerability, and social vulnerability. More vulnerability factors could be considered to analyze tsunami risk change.

5. Conclusions

This study analyzed the tsunami risk change in Qidong County based on LULC classification. The tsunami hazard was evaluated by analyzing three magnitude 9.0 earthquakes in the Ryukyu Trench. Tsunami inundation was calculated using a tsunami numerical model. Tsunami hazard analysis defined the spatial scope of tsunami risk analysis.

Remote sensing was used for tsunami vulnerability analysis. The RF method, which was used for LULC classification, enabled rapid and accurate modeling based on sample training and analyzed LULC based on the model. A number of bands and spectral index combinations were tested to ensure the accuracy of land use classification. The analysis results show that the band combinations should be selected according to the month and season to improve the classification accuracy. In addition, suitable spectral indices could improve the accuracy of land use classification.

According to the results of LULC classification, built-up land in the inundation area of Qidong County increased by 16.62 km^2 from 2013 to 2022. The risk change analysis results show that in the case of a magnitude 9.0 earthquake in the middle of the Ryukyu Trench, the area at tsunami risk level 1 in Qidong County increased by 4.57 km^2 from 2013 to 2022. The area at tsunami risk level 1 area was along the coastal area. With the ongoing economic development of Qidong County, the coastal population and urbanization process have accelerated, resulting in the expansion of urban construction land and an increase in tsunami risk. Our method is important for tsunami disaster mitigation in Qidong County, and can also be applied to other regions with potential tsunami risk. This study conducted tsunami change analysis for five main land use types. However, if there is a children's summer camp in the woodland, the tsunami risk will increase. Therefore, more detailed risk change analysis should be carried out in the future.

The occurrence of a tsunami disaster is inevitable, but the loss caused by disasters can be mitigated through reasonable disaster prevention measures. Tsunami mitigation awareness is an important part of tsunami disaster prevention. Educating the public about tsunami risk can popularize tsunami disaster observation and prevention, enhancing the public's awareness of disaster prevention and mitigation. In addition, tsunami warning exercises should be carried out irregularly to practice the production and dissemination of tsunami warning information, in order to improve participation with tsunami warning in-

stitutions and government departments. Tsunami evacuation and other disaster responses should be studied. Tsunami evacuation plans should be developed and issued to help citizens cope with tsunami disasters.

Author Contributions: Conceptualization, J.H. and Y.G.; data curation, Y.G. and J.W.; formal analysis, T.F. and Y.W.; methodology, J.H. and P.W.; writing, J.H. and W.L. All authors have read and agreed to the published version of the manuscript.

Funding: This research was funded by the Development of Indonesia-China Center for Ocean & Climate (No. 121152000000210003) and the National Key R&D Program of China (No. 2022YFC3003804).

Institutional Review Board Statement: Not applicable.

Informed Consent Statement: Not applicable.

Data Availability Statement: Not applicable.

Conflicts of Interest: The authors declare no conflict of interest.

References

1. Titov, V.; Rabinovich, A.; Mofjeld, H.; Thomson, R.; González, F. The global reach of the 26 December 2004 Sumatra tsunami. *Science* **2005**, *309*, 2045–2048. [CrossRef] [PubMed]
2. Wei, Y.; Newman, A.; Hayes, G.; Titov, V.; Tang, L. Tsunami forecast by joint inversion of real-time tsunami waveforms and seismic or GPS data: Application to the Tohoku 2011 tsunami. *Pure Appl. Geophys.* **2014**, *171*, 3281–3305. [CrossRef]
3. Liu, H.; Zhao, X.; Wang, B. Development and application of high order Boussinesq model in tsunami studies. *J. Hydrodyn. Ser. B* **2010**, *22*, 993–998. [CrossRef]
4. Wei, Y.; Chamberlin, C.; Titov, V.; Tang, L.; Bernard, E. Modeling of the 2011 Japan tsunami: Lessons for near-field forecast. *Pure Appl. Geophys.* **2013**, *170*, 1309–1331. [CrossRef]
5. Baptista, M.; Miranda, P.; Miranda, J.; Victor, L. Constrains on the source of the 1755 Lisbon tsunami inferred from numerical modelling of historical data on the source of the 1755 Lisbon tsunami. *J. Geodyn.* **1998**, *25*, 159–174. [CrossRef]
6. Van Dorn, W. Source mechanism of the tsunami of March 28, 1964 in Alaska. In Proceedings of the Ninth International Conference on Coastal Engineering, Lisbon, Portugal, June 1964; pp. 166–190.
7. Gusman, A.; Supendi, P.; Nugraha, A.; Power, W.; Latief, H.; Sunendar, H.; Widiyantoro, S.; Daryono; Wiyono, S.; Hakim, A.; et al. Source model for the tsunami inside Palu Bay following the 2018 Palu earthquake, Indonesia. *Geophys. Res. Lett.* **2019**, *46*, 8721–8730. [CrossRef]
8. Carvajal, M.; Sepúlveda, I.; Gubler, A.; Garreaud, R. Worldwide signature of the 2022 Tonga volcanic tsunami. *Geophys. Res. Lett.* **2022**, *49*, e2022GL098153. [CrossRef]
9. Hou, J.; Li, X.; Yuan, Y.; Wang, P. Tsunami hazard assessment along the Chinese mainland coast from earthquakes in the Taiwan region. *Nat. Hazards* **2016**, *81*, 1269–1281.
10. Li, L.; Switzer, A.; Chan, C.; Wang, Y.; Weiss, R.; Qiu, Q. How heterogeneous coseismic slip affects regional probabilistic tsunami hazard assessment: A case study in the South China Sea. *J. Geophys. Res. Solid Earth* **2016**, *121*, 6250–6272. [CrossRef]
11. Ren, Z.; Liu, H.; Zhao, X.; Wang, B.; An, C. Effect of kinematic fault rupture process on tsunami propagation. *Ocean Eng.* **2019**, *181*, 43–58. [CrossRef]
12. Wang, Y.; Satake, K.; Sandanbata, O.; Maeda, T.; Su, H. Tsunami data assimilation of cabled ocean bottom pressure records for the 2015 Torishima volcanic tsunami earthquake. *J. Geophys. Res. Solid Earth* **2019**, *124*, 10413–10422. [CrossRef]
13. Ren, Z.; Gao, Y.; Ji, X.; Hou, J. Deterministic tsunami hazard assessment and zoning approach using far-field and near-field sources: Study of Cixi County of Zhejiang Province, China. *Ocean Eng.* **2022**, *247*, 110487. [CrossRef]
14. Hou, J.; Li, X.; Wang, P.; Wang, J.; Ren, Z. Hazard analysis of tsunami disaster on the Maritime Silk Road. *Acta Oceanolog. Sin.* **2020**, *39*, 74–82. [CrossRef]
15. Yuan, Y.; Li, H.; Wei, Y.; Shi, F.; Wang, Z.; Hou, J.; Wang, P.; Xu, Z. Probabilistic Tsunami Hazard Assessment (PTHA) for Southeast Coast of Chinese Mainland and Taiwan Island. *J. Geophys. Res. Solid Earth* **2021**, *126*, e2020JB020344. [CrossRef]
16. Løvholt, F.; Glimsdal, S.; Harbitz, C.; Horspool, N.; Smebye, H.; De Bono, A.; Nadim, F. Global tsunami hazard and exposure due to large co-seismic slip. *Int. J. Disaster Risk Reduct.* **2014**, *10*, 406–418. [CrossRef]
17. Hui, C.; Ning, L.; Cheng, C. Risk Assessment of Tsunamis Along the Chinese Coast Due to Earthquakes. *Int. J. Disaster Risk Sci.* **2022**, *13*, 275–290. [CrossRef]
18. Römer, H.; Willroth, P.; Kaiser, G.; Vafeidis, A.; Ludwig, R.; Sterr, H.; Revilla Diez, J. Potential of remote sensing techniques for tsunami hazard and vulnerability analysis–a case study from Phang-Nga province, Thailand. *Nat. Hazards Earth Syst. Sci.* **2012**, *12*, 2103–2126. [CrossRef]
19. Suppasri, A.; Koshimura, S.; Matsuoka, M.; Gokon, H.; Kamthonkiat, D. Application of remote sensing for tsunami disaster. In *Remote Sensing of Planet Earth*; European Commission: Brussels, Belgium, 2012; pp. 143–168. Available online: https://pdfs.semanticscholar.org/ba6a/c46af8a9ee9b095bb4ee165a166beac598c0.pdf (accessed on 2 September 2022).

20. Eckert, S.; Jelinek, R.; Zeug, G.; Krausmann, E. Remote sensing-based assessment of tsunami vulnerability and risk in Alexandria, Egypt. *Appl. Geogr.* **2012**, *32*, 714–723. [CrossRef]
21. Mas, E.; Koshimura, S.; Suppasri, A.; Matsuoka, M.; Matsuyama, M.; Yoshii, T.; Jimenez, F.; Yamazaki, F.; Imamura, F. Developing Tsunami fragility curves using remote sensing and survey data of the 2010 Chilean Tsunami in Dichato. *Nat. Hazards Earth Syst. Sci.* **2012**, *12*, 2689–2697. [CrossRef]
22. Chaves, M.; Picoli, M.; Sanches, I. Recent applications of Landsat 8/OLI and Sentinel-2/MSI for land use and land cover mapping: A systematic review. *Remote Sens.* **2020**, *12*, 3062. [CrossRef]
23. Tesfaye, B.; Lengoiboni, M.; Zevenbergen, J.; Simane, B. Mapping Land Use Land Cover Changes and Their Determinants in the Context of a Massive Free Labour Mobilisation Campaign: Evidence from South Wollo, Ethiopia. *Remote Sens.* **2021**, *13*, 5078. [CrossRef]
24. Ye, J.; Hu, Y.; Zhen, L.; Wang, H.; Zhang, Y. Analysis on Land-Use Change and its driving mechanism in Xilingol, China, during 2000–2020 using the google earth engine. *Remote Sens.* **2021**, *13*, 5134. [CrossRef]
25. Hua, L.; Zhang, X.; Chen, X.; Yin, K.; Tang, L. A feature-based approach of decision tree classification to map time series urban land use and land cover with Landsat 5 TM and Landsat 8 OLI in a Coastal City, China. *ISPRS Int. J. Geo-Inf.* **2017**, *6*, 331. [CrossRef]
26. Knight, E.; Kvaran, G. Landsat-8 operational land imager design, characterization and performance. *Remote Sens.* **2014**, *6*, 10286–10305. [CrossRef]
27. Masek, J.; Wulder, M.; Markham, B.; McCorkel, J.; Crawford, C.; Storey, J.; Jenstrom, D. Landsat 9: Empowering open science and applications through continuity. *Remote Sens. Environ.* **2020**, *248*, 111968. [CrossRef]
28. Al-Shaibah, B.; Liu, X.; Zhang, J.; Tong, Z.; Zhang, M.; El-Zeiny, A.; Faichia, C.; Hussain, M.; Tayyab, M. Modeling Water Quality Parameters Using Landsat Multispectral Images: A Case Study of Erlong Lake, Northeast China. *Remote Sens.* **2021**, *13*, 1603. [CrossRef]
29. Hamuna, B.; Kalor, J.; Tablaseray, V. The impact of tsunami on mangrove spatial change in eastern coastal of Biak Island, Indonesia. *J. Ecol. Eng.* **2019**, *20*, 1–6. [CrossRef]
30. Deng, Z.; Zhu, X.; He, Q.; Tang, L. Land use/land cover classification using time series Landsat 8 images in a heavily urbanized area. *Adv. Space Res.* **2019**, *63*, 2144–2154. [CrossRef]
31. Ping, B.; Meng, Y.; Su, F. An enhanced linear spatio-temporal fusion method for blending Landsat and MODIS data to synthesize landsat-like imagery. *Remote Sens.* **2018**, *10*, 881. [CrossRef]
32. Sui, Y.; Fu, D.; Wang, X.; Su, F. Surface water dynamics in the North America Arctic based on 2000–2016 Landsat data. *Water* **2018**, *10*, 824. [CrossRef]
33. Paulik, R.; Lane, E.; Williams, S.; Power, W. Changes in tsunami risk to residential buildings at Omaha Beach, New Zealand. *Geosciences* **2019**, *9*, 113. [CrossRef]
34. Ren, Z.; Hou, J.; Wang, P.; Wang, Y. Tsunami resonance and standing waves in Hangzhou Bay. *Phys. Fluids.* **2021**, *33*, 81702. [CrossRef]
35. Nakamura, M. Fault model of the 1771 Yaeyama earthquake along the Ryukyu Trench estimated from the devastating tsunami. *Geophys. Res. Lett.* **2009**, *36*, L19307. [CrossRef]
36. Hsu, Y.; Ando, M.; Yu, S.; Simons, M. The potential for a great earthquake along the southernmost Ryukyu subduction zone. *Geophys. Res. Lett.* **2012**, *39*, L14302. [CrossRef]
37. Ando, M.; Kitamura, A.; Tu, Y.; Ohashi, Y.; Imai, T.; Nakamura, M.; Ikuta, R.; Miyairi, Y.; Yokoyama, Y.; Shishikura, M. Source of high tsunamis along the southernmost Ryukyu trench inferred from tsunami stratigraphy. *Tectonophysics* **2018**, *722*, 265–276. [CrossRef]
38. Skakun, S.; Franch, B.; Vermote, E.; Roger, J.-C.; Becker-Reshef, I.; Justice, C.; Kussul, N. Early season large-area winter crop mapping using MODIS NDVI data, growing degree days information and a Gaussian mixture model. *Remote Sens. Environ.* **2017**, *195*, 244–258. [CrossRef]
39. Rouse, J.; Haas, R.; Schell, J.; Deering, D. Monitoring vegetation systems in the great plains with ERTS. *Third ERTS Symp.* **1973**, *8*, 1.
40. Xu, H. A study on information extraction of water body with the modified normalized difference water index (MNDWI). *J. Remote Sens.* **2005**, *9*, 589–595.
41. Szabó, S.; Gácsi, Z.; Balázs, B. Specific features of NDVI, NDWI and MNDWI as reflected in land cover categories. *Landsc. Environ.* **2016**, *10*, 194–202. [CrossRef]
42. Zha, Y.; Ni, S.; Yang, S. An effective approach to automatically extract urban land-use from TM imagery. *J. Remote Sens. Beijing* **2003**, *7*, 37–40.
43. Rikimaru, A. LAMDSAT TM data processing guide for forest canopy density mapping and monitoring model. In Proceedings of the ITTO Workshop on Utilization of Remote Sensing in Site Assessment and Planning for Rehabilitation of Logged-over Forest, Bangkok, Thailand, July 30–1 August 1996.
44. Liu, P.; Cho, Y.; Yoon, S.; Seo, S. Numerical simulations of the 1960 Chilean tsunami propagation and inundation at Hilo, Hawaii. In *Tsunami: Progress in Prediction, Disaster Prevention and Warning*; Springer: Dordrecht, The Netherlands, 1995; pp. 99–115.
45. Wang, X.; Liu, P. An analysis of 2004 Sumatra earthquake fault plane mechanisms and Indian Ocean tsunami. *J. Hydraul. Res.* **2006**, *44*, 147–154. [CrossRef]

46. Aburas, M.; Ahamad, M.; Omar, N. Spatio-temporal simulation and prediction of land-use change using conventional and machine learning models: A review. *Environ. Monit. Assess.* **2019**, *191*, 1–28. [CrossRef] [PubMed]
47. Litjens, G.; Kooi, T.; Bejnordi, B.; Setio, A.; Ciompi, F.; Ghafoorian, M.; Van der Laak, J.; Ginneken, B.; Sánchez, C. A survey on deep learning in medical image analysis. *Med. Image Anal.* **2017**, *42*, 60–88. [CrossRef] [PubMed]
48. Abdi, A. Land cover and land use classification performance of machine learning algorithms in a boreal landscape using Sentinel-2 data. *GISci. Remote Sens.* **2020**, *57*, 1–20. [CrossRef]
49. Breiman, L. Random forests. *Mach. Learn* **2001**, *45*, 5–32. [CrossRef]
50. Immitzer, M.; Atzberger, C.; Koukal, T. Tree Species Classification with Random Forest Using Very High Spatial Resolution 8-BandWorldView-2 Satellite Data. *Remote Sens.* **2012**, *4*, 2661–2693. [CrossRef]
51. Sambah, A.; Miura, F.; Febriana, A. Geospatial Model of Physical and Social Vulnerability for Tsunami Risk Analysis. *GEOMATE J.* **2019**, *17*, 29–34. [CrossRef]
52. Løvholt, F.; Setiadi, N.; Birkmann, J.; Harbitz, C.; Bach, C.; Fernando, N.; Kaiser, G.; Nadim, F. Tsunami risk reduction–are we better prepared today than in 2004? *Int. J. Disaster Risk Reduct.* **2014**, *10*, 127–142. [CrossRef]
53. Jelínek, R.; Krausmann, E.; Gonzalez, M.; Alvarez-Gomez, J.; Birkmann, J.; Welle, T. Approaches for tsunami risk assessment and application to the city of Cádiz, Spain. *Nat. Hazards* **2012**, *60*, 273–293. [CrossRef]